Quantitative PET/MR imaging of lung cancer in the presence of artifacts in the MR-based attenuation correction maps

Abstract

Background: Positron emission tomography (PET)/magnetic resonance (MR) imaging may become increasingly important for assessing tumor therapy response. A prerequisite for quantitative PET/MR imaging is reliable and repeatable MR-based attenuation correction (AC).

Purpose: To investigate the frequency and test-retest reproducibility of artifacts in MR-AC maps in a lung cancer patient cohort and to study the impact of artifact corrections on PET-based tumor quantification.

Material and Methods: Twenty-five lung cancer patients underwent single-day, test-retest, ^{18}F-fluorodeoxyglucose (FDG) PET/MR imaging. The acquired MR-AC maps were inspected for truncation, susceptibility and tissue inversion artifacts. An anatomy-based bone template and a PET-based estimation of truncated arms were employed, while susceptibility artifacts were corrected manually. We report the frequencies of artifacts and the relative difference (RD) on standardized uptake value (SUV) based quantification in PET images reconstructed with the corrected AC maps.

Results: Truncation artifacts were found in all 50 acquisitions (100%), while susceptibility and tissue inversion artifacts were observed in 6 (12%), and 26 (52%) of the scans, respectively. The RD in lung tumor SUV was less than 5% from bone and truncation corrections, while up to 20% RD was introduced after susceptibility artifact correction, with large inconsistencies between test-retest scans.

Conclusion: The absence of bone and truncation artifacts have limited effect on the PET quantification of lung lesions. In contrast, susceptibility artifacts caused significant and inconsistent underestimations of the lung tumor SUVs, between test-retest scans. This may have clinical implications for patients undergoing serial imaging for tumor therapy response assessment.

Keywords

PET/MR; lung cancer; attenuation correction; artifacts

Introduction

Lung cancer is the most frequent cancer type and the leading cause of cancer-related death in the world (1). Positron emission tomography (PET)/computed tomography (CT) with ^{18}F-fluorodeoxyglucose (FDG) is the standard of care today for lung cancer staging, and is also increasingly used to aid in radiotherapy treatment planning and for tumor therapy response assessment (2, 3, 4, 5, 6).

The recent introduction of integrated PET/magnetic resonance (MR) systems has opened new possibilities for tumor characterization by adding excellent soft-tissue contrast, provided by MR imaging, to the functional information from PET. In this way, simultaneous, multiparametric images can be acquired, that facilitate precision medicine and personalized treatment of the disease (7, 8). The use of non-ionizing MR imaging is another benefit for the use of PET/MR, rather than PET/CT, in the follow-up assessment of patients undergoing radiation or chemotherapy (9).

The reproducibility of the standardized uptake values (SUV) in PET/MR imaging is important for a reliable assessment of therapy response, and it is strongly linked to accurate MR-based attenuation correction (AC) during PET image reconstruction (7, 10, 11, 12, 13). In fully-integrated PET/MR systems, standard AC maps are calculated from the segmentation of MR-images into a number of tissue-classifications (e.g. air, lung, fat and soft tissue), thereby assigning a specific attenuation coefficient to each tissue (7, 14). A known limitation of many MR sequences used for generating AC maps is the low bone signal, which may cause an underestimation of quantitative measurements in the resulting PET images in close vicinity

to osseous tissue (11). Furthermore, the reduced transaxial field of view (FOV) of the MR, in comparison with the PET FOV, has been reported to result in truncation artifacts of distal body parts (15). In addition, distortion of the magnetic field, caused by metallic implants, such as surgical sternal wires, may cause susceptibility artifacts in the AC maps (16, 17). Lastly, soft-fat tissue inversions in the AC map may occur (16). These effects have been proven to affect both diagnostic quality, and hinder accurate quantification of the tracer-distribution in brain, head/neck, and cardiac PET studies (16, 17). Further, a recent study reported that MR-AC related artifacts occurred frequently and inconsistently in test-retest scans of lung cancer patients, leading to non-consistent SUV quantification in serial examinations (18).

The aim of the current study is to investigate the frequency and the test-retest reproducibility of artifacts observed in standard MR-based AC maps in a lung cancer patient cohort undergoing PET/MR imaging. Further, we intend to correct for artifacts in the AC maps and evaluate the impact of the corrections on the PET-based quantification in the test-retest setup.

Materials and Methods

Ethical approval

This study was approved by the [redacted] Regional Committees for Medical and Health Research Ethics ([redacted] reference [redacted]). All patients signed written informed consent.

Patient population, preparation and imaging overview

Twenty-five lung cancer patients with a total of 26 lung lesions were included in this single-injection dual-time point PET/MR imaging study. Patients fasted 15h ± 4h before the injection

of 281 MBq ± 41 MBq FDG. PET/MR assessment started 113 min ± 10 min post FDG injection (Fig. 1).

PET/MR image acquisition

The PET/MR acquisitions were performed in a Siemens Biograph mMR (software version VB20P) (Siemens Healthineers, Erlangen, Germany) using a free breathing and arms down scan protocol during the entire simultaneous image acquisition. All patients had the same anatomical region scanned twice, without repositioning and reinjection between the scans, thus, allowing for the assessment of the test-retest reproducibility of the images. First, a 10 minute, 1-bed position scan, centered over mediastinum, was performed, immediately followed by another 10 minute, 2-bed position scan of the whole thorax (Fig. 1). A standard DIXON-based MR-AC map was acquired for each scan, resulting in a total of 50 MR-AC maps for the 25 patients.

Inspection of the attenuation correction maps

All 50 MR-AC maps were inspected for artifacts by two experienced imaging physicists. We report the frequency of the observed artifacts from this test-retest assessment, divided into three categories: truncation artifacts, susceptibility artifacts in the sternum, and tissue inversion (Fig. 2, A-C). For the second category, we specify the number of acquisitions for which lung segmentation in the MR-AC map failed.

Corrections of the attenuation correction maps

For each patient, up to four additional sets of test-retest AC maps were formed by correcting for the artifacts that were found in each original AC map (Fig. 2, D-F): 1) Missing bone was

corrected by adding an anatomy-based bone template of the spine (19); 2) Truncation artifacts, if found, were corrected using the MLAA algorithm (20). Both these corrections were performed using vendor-provided software, thus, updating the AC maps in DICOM-format; 3) Susceptibility artifacts, causing misclassified voxels in the sternum and lungs, if found, were corrected using an in-house developed algorithm implemented in Matlab (Mathworks, MA, USA) (17). This correction was applied on the interfiles used for reconstructions in a vendor-provided reconstruction tool (JSRecon (e7-tools), Siemens Healthineers, Erlangen, Germany); 4) A fully-corrected AC map was formed by applying all the above-mentioned corrections. The different AC maps are denoted $AC_{Original}$, AC_{Bone}, AC_{Trunc}, AC_{Susc} and AC_{All}, respectively, throughout this paper. Thus, for each patient, a total of 8 (no AC_{Susc}) or 10 (with AC_{Susc}) different AC maps were included for subsequent analyses.

PET image reconstruction

Static PET images were reconstructed for all patients by employing each of the generated AC map, to form $PET_{Original}$, PET_{Bone}, PET_{Trunc}, PET_{Susc} and PET_{All} (Fig. 3). This resulted in a total of 214 PET image series included for further evaluation. All reconstructions were performed using ordered-subset expectation-maximization (OSEM) algorithm with 3 iterations, 21 subsets and 4mm Gaussian smoothing. The matrix size of the reconstructed PET images was 344×344×224 and 344×344×127 for test (2 bed) and retest (1 bed) scans, respectively, with a voxel size of 2.1×2.1×2.0 mm.

PET image evaluation

FDG-avid lesions were delineated using a 41% SUV_{max} threshold (21). For each lesion the mean, maximum and peak SUV values were measured (SUV_{mean}, SUV_{max} and SUV_{peak}).

Relative difference (RD) was calculated using Equation 1,

$$RD = \left[\frac{SUV_{Corrected}}{SUV_{Original}} - 1\right] \times 100\% \quad (1)$$

where $SUV_{Corrected}$ and $SUV_{Original}$ represent measurements obtained from the PET images reconstructed with the corrected and original AC maps, respectively (Fig. 3). Statistical significance was calculated using Wilcoxon signed-rank test, after square root transformation of the data, to correct for asymmetric distributions.

The impact of the corrections on tumor size was evaluated by measuring the largest diameter and the volume of the delineated lesions in all reconstructed images.

Results

Frequency of artifacts

Truncation artifacts were reported in all 50 MR-AC maps (100%), whereas susceptibility artifacts, caused by sternal wires, and tissue inversion was observed in 6 (12%) and 26 (52%) of the MR-AC map, respectively. All susceptibility artifacts were reproducible between test-retest scans. As a consequence of susceptibility artifacts in the sternum, lung tissue segmentation failed for two of the patients in the test scan (Table 1).

Tissue inversion artifacts were observed in a total of 19 (76%) patients, which was reproduced in the retest scan in 7 (37%) of the patients. For 12 (63%) of the patients, tissue inversion artifacts were present in only one of either the test or retest scans (Table 1).

Correction of artifacts

The relative differences of the lung tumor SUVs after applying bone, truncation and all corrections are shown in Figure 4. Inclusion of the anatomy-based bone template caused an

increased tumor SUV_{mean}, SUV_{max} and SUV_{peak} of less than 0.5% ($p<0.001$) in both test and retest scans, while correction of truncation, and all artifacts yielded a corresponding increase of less than 3% ($p<0.01$) (Fig. 4).

Table 2 shows the relative difference in the lung tumor SUV for the three patients with susceptibility artifacts in the AC maps after applying the different corrections. The susceptibility artifacts introduced an acquisition-varying effect on the tumor SUV values, with test-retest variations of up to 22% (Patient 21).

To visualize the effect of the different AC map corrections on the reconstructed PET images, relative difference images of a representative patient is shown in Figure 5, and Supplementary Figures S1 and S2.

Figure 6 shows the association between the SUV and lesion diameter, without and with corrections for artifacts in the AC maps. While the corrections affected the SUV values, they did not introduce alterations in the tumor diameters (Table 3). Similar results were obtained for the tumor volumes (Table 3 and Fig. 7).

Discussion

We have studied how individual and combined corrections of the three most frequent artifacts (absence of bone, truncation of arms, and susceptibility artifacts) in standard DIXON-MR-AC maps affect lesion quantification in a PET/MR imaging cohort of lung cancer patients. Our main finding is that artifacts in the MR-AC maps introduce variability in the lung lesion SUVs of up to 22% in a test-retest set-up without patient repositioning. Absence of bone is caused by known limitations in the MR DIXON scan sequence, and, therefore, is present in all scans (11). The impact of adding the anatomy-based bone template on the lung tumor SUVs was low (<0.5%) (Fig. 4), and the effect is limited to the close vicinity of the spine (Fig. 5). This concord with earlier studies that showed only local effect close to the bones, and no

clinically relevant effects for lung lesions, when omitting bone from the AC map (14, 22, 23).

Truncation artifacts were observed in all AC maps. These artifacts arise from fixed geometrical limitations in the MR FOV, and, thus, are not expected to affect test-retest examinations. This is also in agreement with an earlier study (17). We found that truncation artifacts introduced up to 3% relative differences in the lung tumor SUV values (Fig. 4), and even larger effects inside the truncated regions (Fig. 5), which is in accordance with previous studies (24, 25). This result indicates that accurate truncation correction of the AC maps is not necessarily critical for clinically relevant lung tumor quantification (6).

The frequency of susceptibility artifacts was reproducible between test-retest scans (Table 1). This agrees with a previous study focusing on artifacts in MR-AC maps for cardiac PET/MR applications (17). However, in the present study we report a reduced frequency of susceptibility artifacts (12%), compared to the previous study (25%). This is due to the fact that cardiac patients have a higher frequency of sternal wires following from cardiac surgeries, compared to lung cancer patients. For two of the acquisitions in our study (Patient 20 and 21, test scan), the susceptibility artifacts in the sternum caused misclassified voxels in parts of the lungs, due to failure of the lung segmentation algorithm. For these scans, the artifact correction, and subsequent filling of the lungs with correct attenuation values, had a large impact (>100%) on the resulting PET SUV values in the lungs (Fig. 5 and Supplementary Fig. S2), and on the corresponding lung tumor SUVs (-5.2% to - 22.1%) (Table 2). For acquisitions with susceptibility artifacts where the lung segmentation was successful, the impact of the corrections on the SUVs were lower (-0.3% to -2.8%) (Table 2 and Supplementary Fig. S1). This demonstrates that the accuracy in the attenuation values of the tissue surrounding a lung lesion is important for accurate tumor quantification, as also reported in an earlier study (19). Furthermore, the importance of correct attenuation values in the sternum, for lesion quantification, was shown in another recent study (26).

The combined effect of the applied corrections for the absence of bone and truncation had only limited effect (RD<3%) on the lung tumors (Fig. 4). However, correcting for susceptibility artifacts, introduced by sternal wires, caused a RD in the lesions of up 28.7% (Table 2), a clinically relevant measure (6), which may affect the treatment assessment of the patient, as the effects from these artifacts were not reproducible between test-retest scans.

We report tissue inversion artifacts in 26 of 50 (52%) acquisitions, with low reproducibility (37%) between test-retest scans (Table 1). Our incidence rate is higher than previously reported for other disease groups (16, 17). Tissue inversion artifacts in the AC maps may introduce up to 35% quantification errors in the affected areas of the PET image (16). In the current study, tissue inversion was observed exclusively in the abdomen of the patient. This explains the higher frequency of tissue inversion in retest scans (2 bed), compared to test scans (1 bed). Because all lung lesions were far away from the affected areas, the impact on tumor quantification was anticipated to be low, and, therefore, no tissue inversion correction was employed in the current study.

In response assessment studies, both lesion size and SUV can be used as measures of therapy response, where one or both may decrease after successful therapy (6). In this study, it was found that the AC map corrections had no impact on the measured lesion diameter or volume (Table 3, Fig. 6 and Fig. 7), thus, lesion size-based assessment of therapy response is independent of AC map artifact corrections. Furthermore, the increase in SUV values due to the corrections were independent of tumor size (Fig. 6 and Fig. 7), however, because the SUV values were increased by the corrections (Fig. 4, Fig. 6, Fig. 7 and Table 2), careful inspection and correction of the AC maps, prior to PET image reconstruction, is still critical in SUV-based response assessment studies.

Our study has several limitations. Bone artifacts were corrected using an anatomy-based bone template (19), which does not model the ribs. However, the effect of the ribs is expected

to be non-significant, due to their breathing-induced shifting during acquisition, and the fact that they are small and mainly consist of trabecular bone (27).

Further, susceptibility artifacts in the MR-AC maps were corrected with a simple, manual method in this study. More advanced, and fully-automatic correction methods, have been proposed earlier (28, 29). However, with the introduction of novel artifact reducing MR sequences (e.g. MAVRIC, VAT, WARP etc.), susceptibility artifacts could be minimized already at acquisition, thus potentially eliminating the need for manual retrospective correction of the AC maps. Unfortunately, such sequences are currently time consuming, which hampers the implementation into clinical routine (30, 31, 32, 33).

While the PET/MR system evaluated in the current study used a DIXON-based sequence for AC, other systems, using non-DIXON-based sequences, may cause other types of errors. However, systems using for example T1-weighted fast gradient-echo sequences, are expected to be prone to similar types of artefacts as the DIXON-based methods.

Another limitation was that different FOVs were used between test and retest scans. However, this is assumed to have minimal effect on the resulting SUV_{mean} and SUV_{peak}, because of their robustness to noise, and because the same lung segmentation algorithm was applied in both 1 and 2 bed scans (14, 34).

Also, we did not investigate the effect of respiratory motion on the MR-AC maps, which is known to introduce large biases in thoracic PET imaging (35, 36, 37).

Lastly, there were relatively small number of patients included in this study.

In conclusion, the majority of artifacts found in the MR-AC maps, in this clinical PET/MR lung cancer study, did not affect the quantitative accuracy of SUV or tumor size measurements. However, susceptibility artifacts may cause clinically relevant variations in lung tumor SUV measurements, which might affect the accuracy in serial studies of the same

patient. Therefore, our findings warrant careful inspection of the MR-AC maps and subsequent correction of susceptibility artifacts, to ensure highest possible diagnostic accuracy of the PET/MR examination.

References

1 Pasic A, Postmus PE, Sutedja TG. What is early lung cancer? A review of the literature. Lung Cancer 2004;45:267–277.

2 Van Elmpt W, Zegers CML, Das M, et al. Imaging techniques for tumour delineation and heterogeneity quantification of lung cancer: Overview of current possibilities. J Thorac Dis 2014;6:319–327.

3 Sauter AW, Schwenzer N, Divine MR, et al. Image-derived biomarkers and multimodal imaging strategies for lung cancer management. Eur J Nucl Med Mol Imaging 2015;42:634–643.

4 Ladrón De Guevara Hernández D. The Role of PET/CT Imaging in Lung Cancer. J Cancer Ther 2015; 6:690–700.

5 Greenspan, S B. Role of PET/CT for precision medicine in lung cancer: perspective of the Society of Nuclear Medicine and Molecular Imaging. Transl Lung Cancer Res 2017;6:617–620.

6 Pinker K, Riedl C, Weber WA. Evaluating tumor response with FDG PET: updates on PERCIST, comparison with EORTC criteria and clues to future developments. Eur J Nucl Med Mol Imaging 2017; 44:55–66.

7 Bezrukov I, Mantlik F, Schmidt H, et al. MR-based PET attenuation correction for PET/MR imaging. Semin Nucl Med 2013;43:45–59.

8 Huo E, Wilson DM, Eisenmenger L, et al. The Role of PET/MR Imaging in Precision Medicine. PET Clin 2017;12:489–501.

9 Lee SM, Goo JM, Park CM, et al. Preoperative staging of non-small cell lung cancer: prospective comparison of PET/MR and PET/CT. Eur Radiol 2016;26:3850–3857.

10 Keller SH, Holm S, Hansen AE, et al. Image artifacts from MR-based attenuation correction in clinical, whole-body PET/MRI. Magn Reson Mater Physics, Biol Med 2013;26:173–181.

11 Bezrukov I, Schmidt H, Mantlik F, et al. MR-Based Attenuation Correction Methods for Improved PET Quantification in Lesions Within Bone and Susceptibility Artifact Regions. J Nucl Med 2013; 54:1768–1774.

12 Wagenknecht G, Kaiser HJ, Mottaghy FM, et al. MRI for attenuation correction in PET: Methods and challenges.

Magn Reson Mater Physics, Biol Med 2013;26:99–113.

13 Reference is blinded.

14 Martinez-Moller A, Souvatzoglou M, Delso G, et al. Tissue Classification as a Potential Approach for Attenuation Correction in Whole-Body PET/MRI: Evaluation with PET/CT Data. J Nucl Med 2009; 50:520–526.

15 Schramm G, Langner J, Hofheinz F, et al. Influence and compensation of truncation artifacts in MR-based attenuation correction in PET/MR. IEEE Trans Med Imaging 2013;32:2056–2063.

16 Ladefoged CN, Hansen AE, Keller SH, et al. Impact of incorrect tissue classification in Dixon-based MR-AC: fat-water tissue inversion. EJNMMI Phys 2014;1:101.

17 Reference is blinded.

18 Olin A, Ladefoged CN, Langer NH, et al. Reproducibility of MR-Based Attenuation Maps in PET/MRI and the Impact on PET Quantification in Lung Cancer. J Nucl Med 2018;59:999–1004.

19 Paulus DH, Quick HH, Geppert C, et al. Whole-Body PET/MR Imaging: Quantitative Evaluation of a Novel Model-Based MR Attenuation Correction Method Including Bone. J Nucl Med 2015;56:1061– 1066.

20 Nuyts J, Bal G, Kehren F, et al. Completion of a truncated attenuation image from the attenuated PET emission data. IEEE Trans Med Imaging 2013;32:237–246.

21 Boellaard R, Delgado-Bolton R, Oyen WJG, et al. FDG PET/CT: EANM procedure guidelines for tumour imaging: version 2.0. Eur J Nucl Med Mol Imaging 2015;42:328–354.

22 Samarin A, Burger C, Wollenweber SD, et al. PET/MR imaging of bone lesions - Implications for PET quantification from imperfect attenuation correction. Eur J Nucl Med Mol Imaging 2012;39:1154–1160.

23 Aznar MC, Sersar R, Saabye J, et al. Whole-body PET/MRI: The effect of bone attenuation during MR-based attenuation correction in oncology imaging. Eur J Radiol 2014;83:1177–1183.

24 Reference is blinded.

25 Mawlawi O, Erasmus JJ, Pan T, et al. Truncation artifact on PET/CT: Impact on measurements of activity concentration and assessment of a correction algorithm. Am J Roentgenol 2006;186:1458–1467.

26 Svirydenka H, Delso G, De Galiza Barbosa F, et al. The Effect of Susceptibility Artifacts Related to Metallic Implants on Adjacent-Lesion Assessment in Simultaneous TOF PET/MR. J Nucl Med 2017; 58:1167–1173.

27 Reference is blinded.

28 Schramm G, Maus J, Hofheinz F, et al. Evaluation and automatic correction of metal-implant-induced artifacts in MR-based attenuation correction in whole-body PET/MR imaging. Phys Med Biol 2014; 59:2713–2726.

29 Ladefoged CN, Andersen FL, Keller SH, et al. Automatic correction of dental artifacts in PET/MRI. J Med Imaging 2015;2:024009.

30 Sutter R, Ulbrich EJ, Jellus V, et al. Reduction of Metal Artifacts in Patients with Total Hip Arthro- plasty with Slice-encoding Metal Artifact Correction and View-Angle Tilting MR Imaging. Radiology 2012;265:204–214.

31 Talbot BS, Weinberg EP. MR Imaging with Metal-suppression Sequences for Evaluation of Total Joint Arthroplasty. Radiographics 2015;36:209–225.

32 Dillenseger JP, Molière S, Choquet P, et al. An illustrative review to understand and manage metal- induced artifacts in musculoskeletal MRI: a primer and updates. Skeletal Radiol 2016;45:677–688.

33 Jungmann PM, Agten CA, Pfirrmann CW, et al. Advances in MRI around metal. J Magn Reson Imaging 2017;46:972–991.

34 Lodge MA, Chaudhry MA, Wahl RL. Noise Considerations for PET Quantification Using Maximum and Peak Standardized Uptake Value. J Nucl Med 2012;53:1041–1047.

35 Werner MK, Parker JA, Kolodny GM, et al. Respiratory gating enhances imaging of pulmonary nodules and measurement of tracer uptake in FDG PET/CT. Am J Roentgenol 2009;193:1640–1645.

36 Liu C, Pierce II LA, Alessio AM, et al. The impact of respiratory motion on tumor quantification and delineation in static PET/CT imaging. Phys Med Biol 2009;54:7345–7362.

37 Apostolova I, Wiemker R, Paulus T, et al. Combined correction of recovery effect and motion blur for SUV quantification of solitary pulmonary nodules in FDG PET/CT. Eur Radiol 2010;20:1868–1877.

Table 1: Frequency of artifacts observed among the test-retest AC maps in the data set. Positive observations are indicated with x.

Patient #	Truncation		Susceptibility		Failed lung seg.		Tissue inversion	
	Test	Retest	Test	Retest	Test	Retest	Test	Retest
1	x	x						
2	x	x					x	x
3	x	x						
4	x	x						
5	x	x						
6	x	x					x	x
7	x	x	x	x				x
8	x	x						x
9	x	x						x
10	x	x						
11	x	x						x
12	x	x					x	x
13	x	x					x	
14	x	x						x
15	x	x					x	x
16	x	x					x	x
17	x	x						x
18	x	x						x
19	x	x						x
20	x	x	x	x	x		x	x
21	x	x	x	x	x			x
22	x	x						x
23	x	x						
24	x	x						x
25	x	x					x	x
Test-Retest sum	25 (100%)	25 (100%)	3 (12%)	3 (12%)	2 (8%)	0 (0%)	8 (32%)	18 (72%)
Total sum	50 (100%)		6 (12%)		2 (4%)		26 (52%)	
Test ∪ Retest	25 (100%)		3 (12%)		2 (4%)		19 (76%)	
Test ∩ Retest	25 (100%)		3 (12%)		0 (0%)		7 (37%)	
(Test ∪ Retest)\(Test ∩ Retest)	0 (0%)		0 (0%)		2 (4%)		12 (63%)	

Table 2: Relative difference in SUV before and after correction of susceptibility, and all artifacts, respectively, for the three patients with susceptibility artifacts in the AC maps. Asterisk (*) indicates values derived from acquisitions where lung segmentation failed and was subsequently corrected.

	Susceptibility artifacts corrected						All artifacts corrected					
	SUV_{mean}		SUV_{max}		SUV_{peak}		SUV_{mean}		SUV_{max}		SUV_{peak}	
Patient #	Test	Retest	Test	Retest	Test	Retest	Test	Retest	Test	Retest	Test	Retest
7	2.2%	1.6%	2.3%	1.5%	2.8%	2.3%	8.3%	5.1%	7.8%	4.0%	8.3%	7.2%
20	6.5%*	1.2%	7.3%*	0.4%	5.2%*	0.3%	10.6%*	0.8%	11.6%*	0.2%	9.4%*	-0.2%
21	20.0%*	1.4%	22.1%*	1.4%	16.1%*	1.2%	25.9%*	4.4%	28.7%*	4.5%	20.7%*	3.8%

Table 3: Tumor diameter and volume without and with corrections for artifacts in the AC maps. Susceptibility artifact corrections of the three patients from Table 2 are not included here. The corrections did not introduce any relevant alterations in the tumor diameters or volumes.

		Absolute difference		
	Original	Bone	Trunc	Bone+Trunc
Volume ≤10 cm^3				
Tumor diameter [mm]	22.5±7.0	0.0±0.1 (p=0.10)	0.1±0.5 (p=0.45)	0.0±0.6 (p=0.98)
MTV [cm^3]	2.8±2.0	0.0±0.0 (p=0.01)	0.0±0.0 (p=0.19)	0.0±0.1 (p=0.60)
Volume > 10 cm^3				
Tumor diameter [mm]	76.7±28.8	0.0±0.0 (p=0.33)	0.1±0.3 (p=0.07)	0.1±0.4 (p=0.55)
MTV [cm^3]	54.6±47.0	0.3±0.8 (p=0.10)	0.6±1.1 (p=0.02)	0.0±1.2 (p=0.87)
All volumes				
Tumor diameter [mm]	43.3±32.4	0.0±0.1 (p=0.07)	0.1±0.4 (p=0.13)	0.0±0.5 (p=0.75)
MTV [cm^3]	22.7±38.4	0.1±0.5 (p=0.09)	0.3±0.8 (p=0.02)	0.0±0.7 (p=0.82)

Figure Legends

Figure 1: Time line of the single-injection dual-time point imaging study. Patients were injected with FDG, followed by 60 minutes rest, before undergoing PET/CT and PET/MR imaging. PET and MR DIXON data that were included in this study are indicated in red and blue color, for the 1-bed position scan centered over mediastinum (test), and the 2-bed position scan of the whole thorax (retest), respectively. The corresponding anatomical regions are indicated approximately on the coronal overview scan to the right.

Figure 2: Examples of the three types of artifacts reported in this study and their corrections in the MR-AC maps: **A** Truncation artifact, where the arms of the patient are outside the MR FOV. **B** Susceptibility artifact caused by surgical sternal wires. Note the failed lung segmentation, where lung attenuation values have been incorrectly assigned to background (red color in the box insert). **C** Tissue inversion artifact with a soft-fat tissue swap. This artifact was not corrected in this study. **D** Correction of truncated arms using the MLAA algorithm (20). **E** Susceptibility artifact correction using an in-house developed algorithm (17). Note that the lungs have been ”filled” with lung attenuation values (yellow color in the box insert). **F** Correction of missing bone by adding an anatomy-based bone template of the spine (19).

Figure 3: Schematic overview of MR-AC map correction, PET image reconstruction and subsequent quantitative SUV extraction. For each patient, up to five different sets of test-retest PET images were reconstructed, using the original AC map ($AC_{Original}$), and each of the corrected AC maps (AC_{Bone}, AC_{Trunc}, AC_{Susc} and AC_{All}). From each PET image, the lung tumor SUV_{mean}, SUV_{max} and SUV_{peak} was extracted from the delineated tumor (41% of SUV_{max} threshold). The analysis was performed for both test and retest scans.

Figure 4: Box plots showing the relative difference in lung lesion SUV_{mean} (top row), SUV_{max} (middle row) and SUV_{peak} (bottom row), obtained from the 41% SUV_{max} threshold, after correcting for bone, truncation and all effects, compared to the original, uncorrected case, for test (left) and retest (right) scans, respectively. Asterisks (*) indicate significance level. ϮCorrections for susceptibility artifacts of the three patients from Table 2 are not included in this column.

Figure 5: The effect of the different corrections in the AC maps on the reconstructed PET images for a representative coronal slice of patient 21. **A** The original PET image. **B** The fully-corrected PET image. **C- F** RD images between original and corrected PET images, where bone correction (**C**), truncation correction (**D**), susceptibility correction (**E**), and all corrections (**F**)), has been applied, respectively. A schematic circumference of the lung lesion for this patient has been indicated with a green line. Of note, the horizontal stripe in the central part of the right lung and the top part of the left lung was caused by transitions between correct and incorrect lung segmentation regions in the MR-AC map.

Figure 6: Lesion diameter without and with all corrections for artifacts in the AC maps. Susceptibility artifact corrections of the three patients from Table 2 are not included here. The corrections did not introduce any relevant alterations in the tumor diameters when using SUV_{mean} (**A**), SUV_{max} (**B**) nor SUV_{peak} (**C**) assessments. Note that because SUV_{peak} is not defined for lesions with volume <1 cm^3, 5 data points were excluded from panel **C**.

Figure 7: Tumor volume without and with all corrections for artifacts in the AC maps. Susceptibility artifact corrections of the three patients from Table 2 are not included here. Data points with volumes <10 cm^3 are shown in the insert. The corrections did not introduce any relevant alternations in the lesion volumes when using SUV_{mean} (**A**), SUV_{max} (**B**) nor SUV_{peak} (**C**) assessments. Note that because SUV_{peak} is not defined for lesions with volume <1 cm^3, 5 data points were excluded from panel **C**.

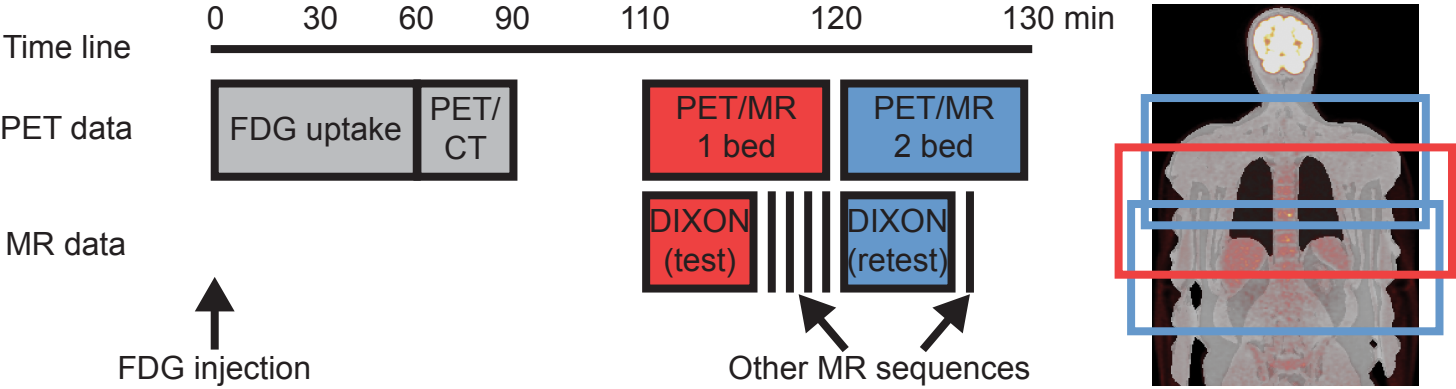
0
30
60
90
110
120
130 min
Time line
PET data
FDG uptake
PET/
CT
PET/MR
1 bed
PET/MR
2 bed
MR data
DIXON
(test)
DIXON
(retest)
FDG injection
Other MR sequences

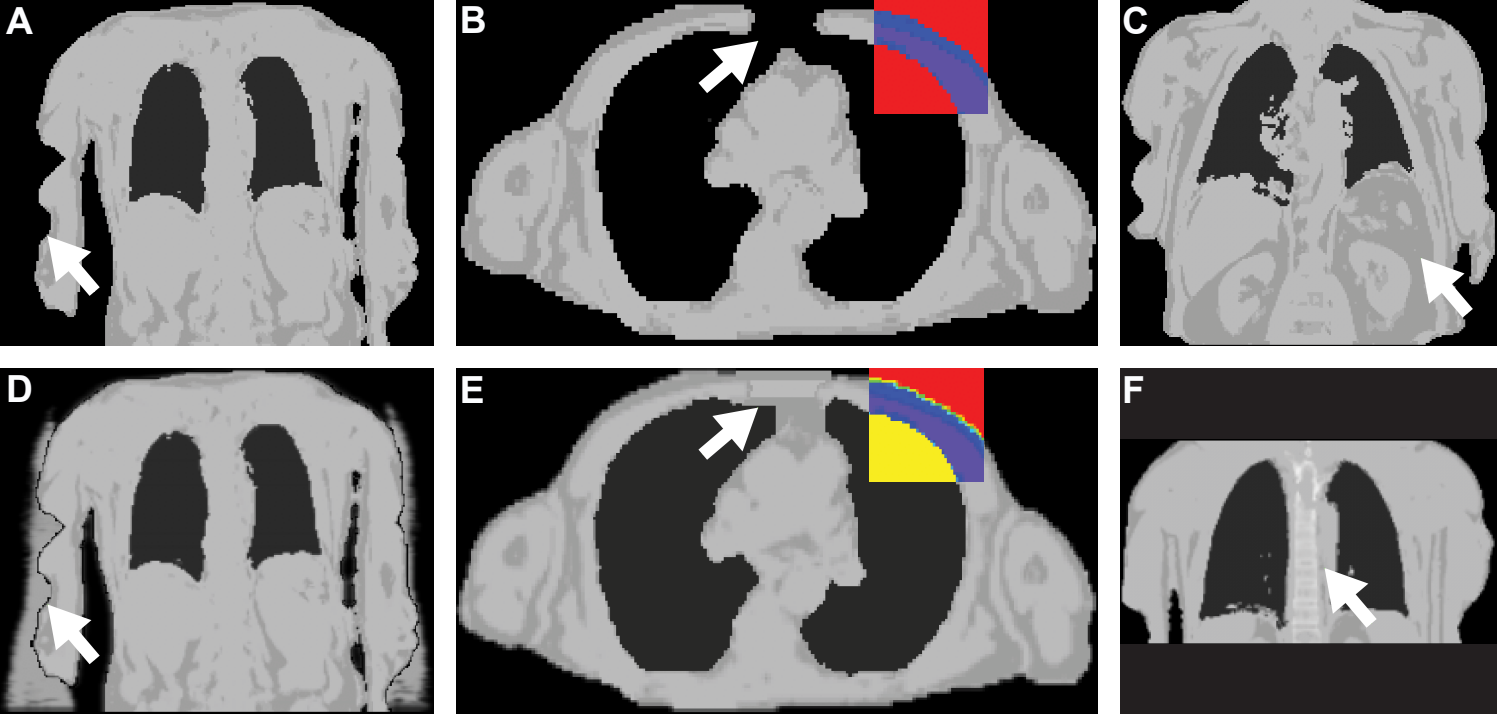
A
B
C
D
E
F

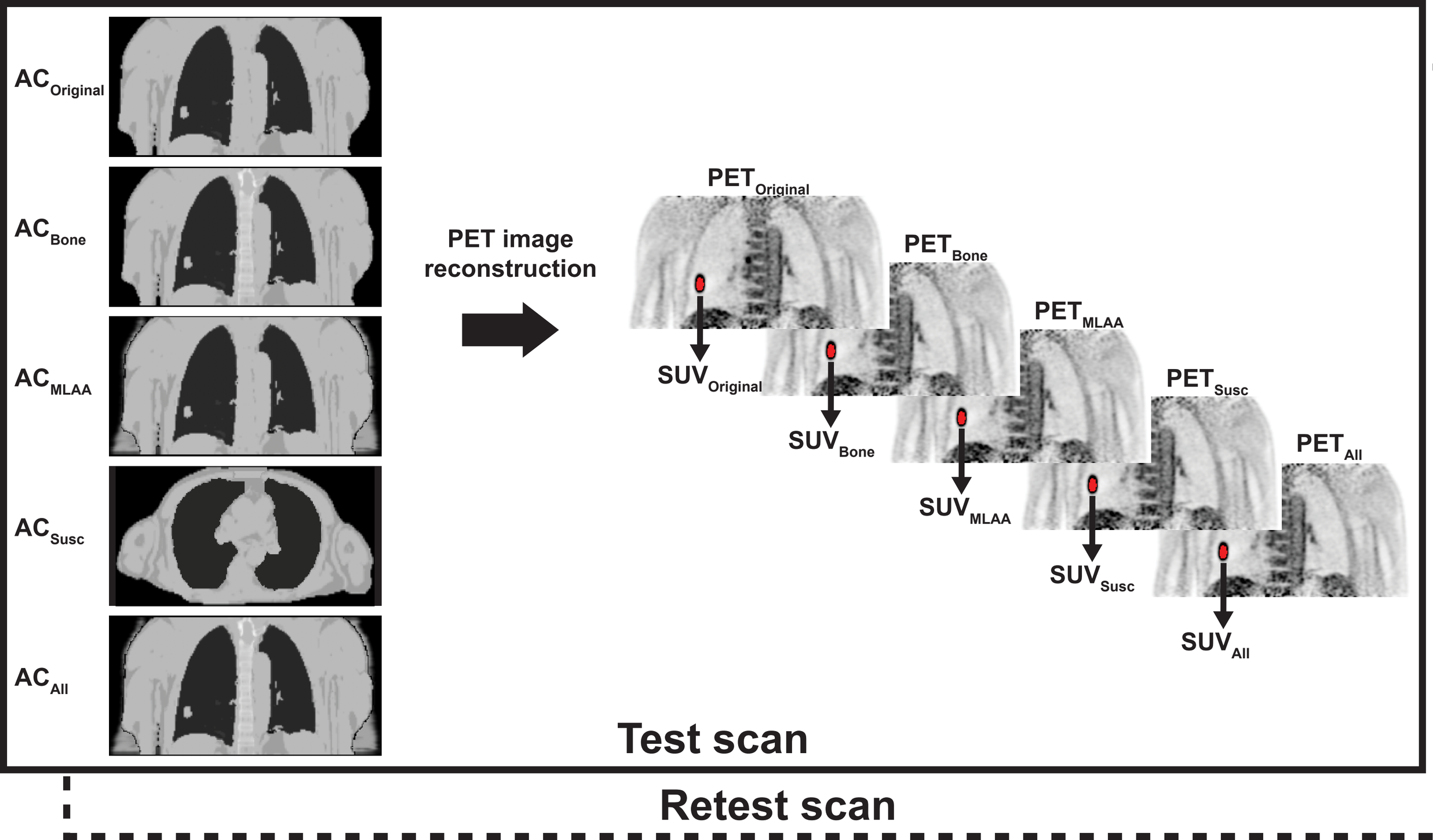
AC Original
AC Bone
AC MLAA
AC Susc
AC All
PET image reconstruction
PET Original
PET Bone
PET MLAA
PET Susc
PET All
SUV Original
SUV Bone
SUV MLAA
SUV Susc
SUV All
Test scan
Retest scan

Test scan

Retest scan

RD in SUV_{mean}

RD in SUV_{max}

RD in SUV_{peak}

8%
6%
4%
2%
0%
-2%
-4%

Original
Bone
MLAA
All†

****
****
****

**
***
***

***
**
**

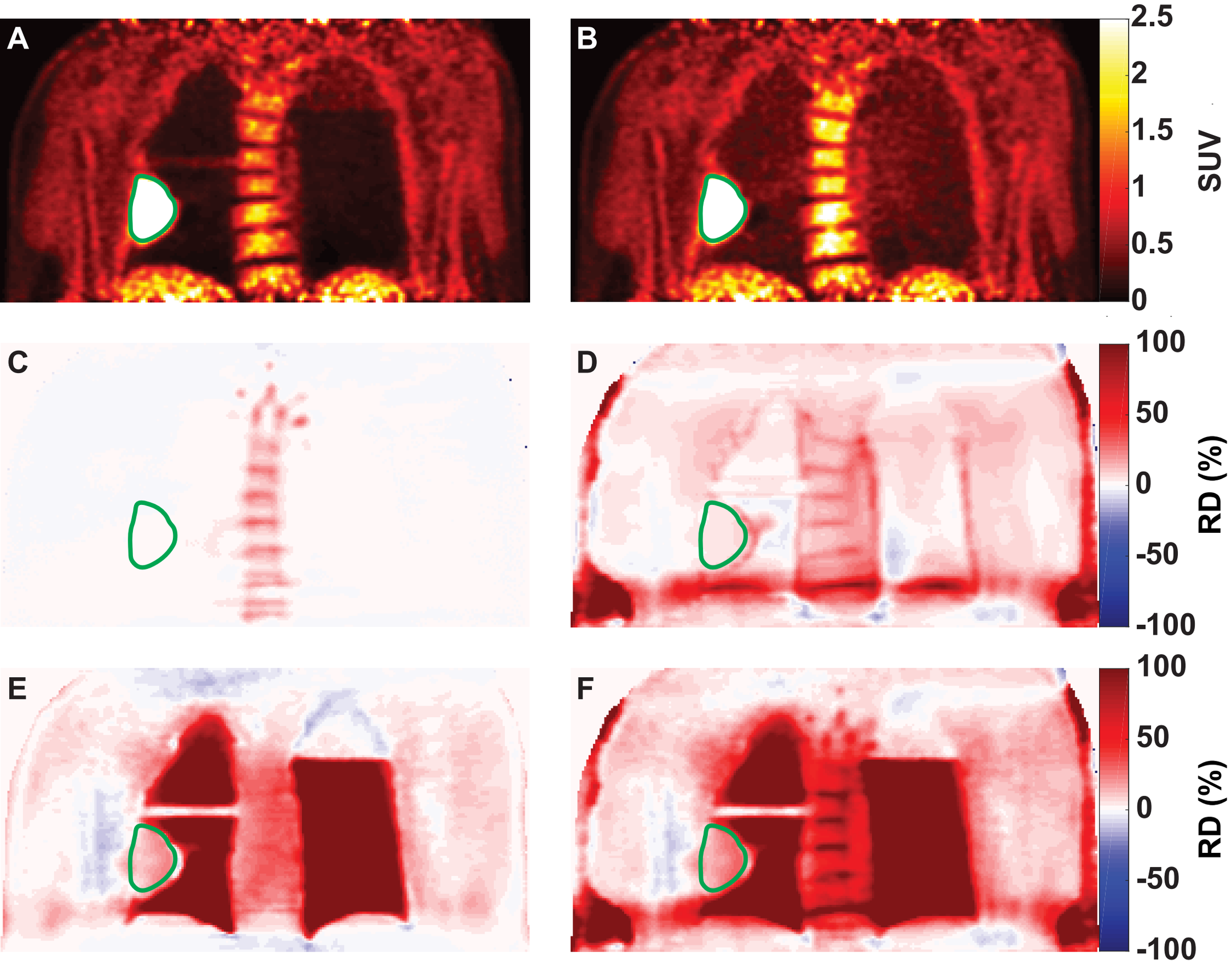
A
B
2.5
2
1.5
1
0.5
0
SUV
C
D
100
50
0
-50
-100
RD (%)
E
F
100
50
0
-50
-100
RD (%)

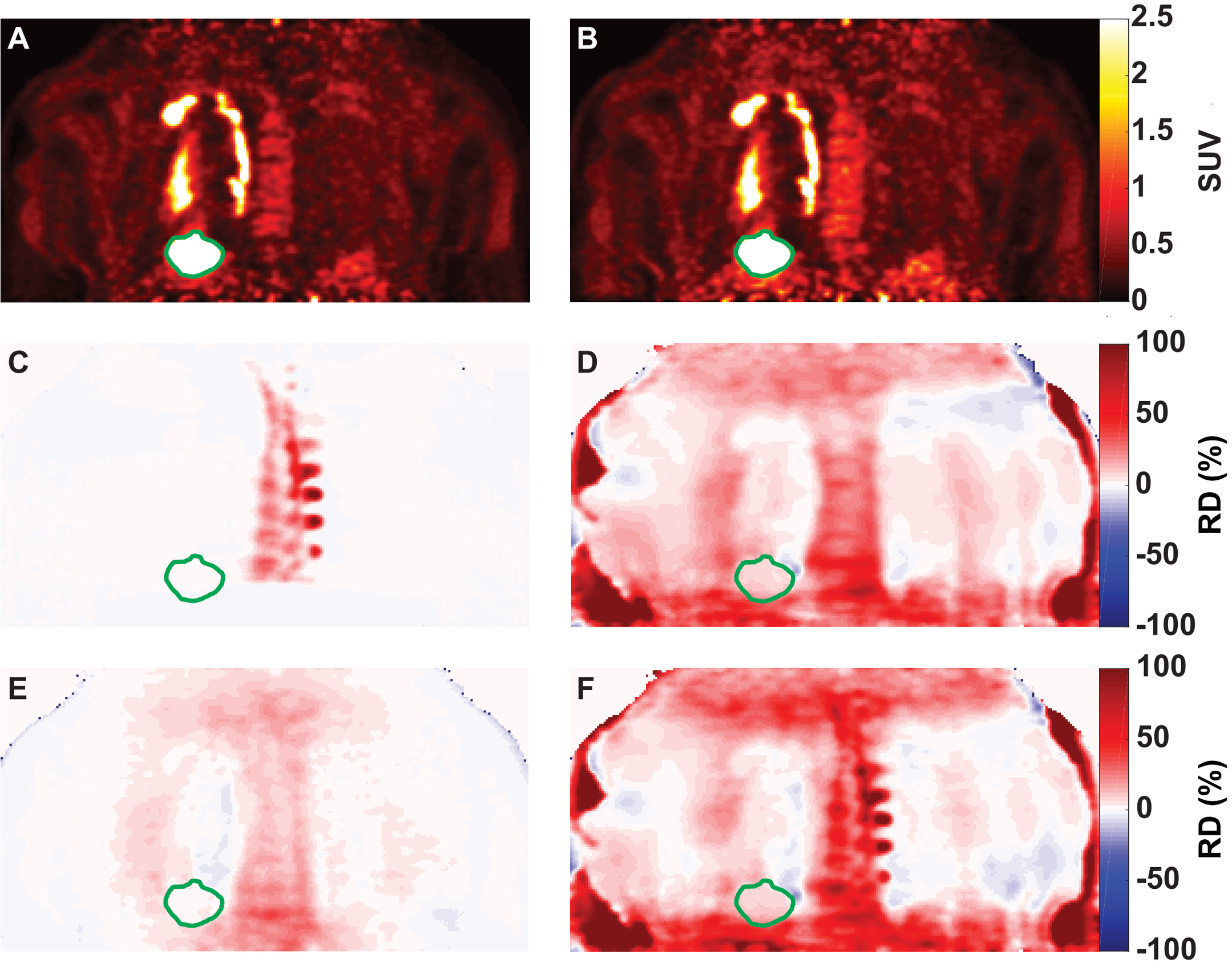
A
B
2.5
2
1.5
1
0.5
0
SUV
C
D
100
50
0
-50
-100
RD (%)
E
F
100
50
0
-50
-100
RD (%)

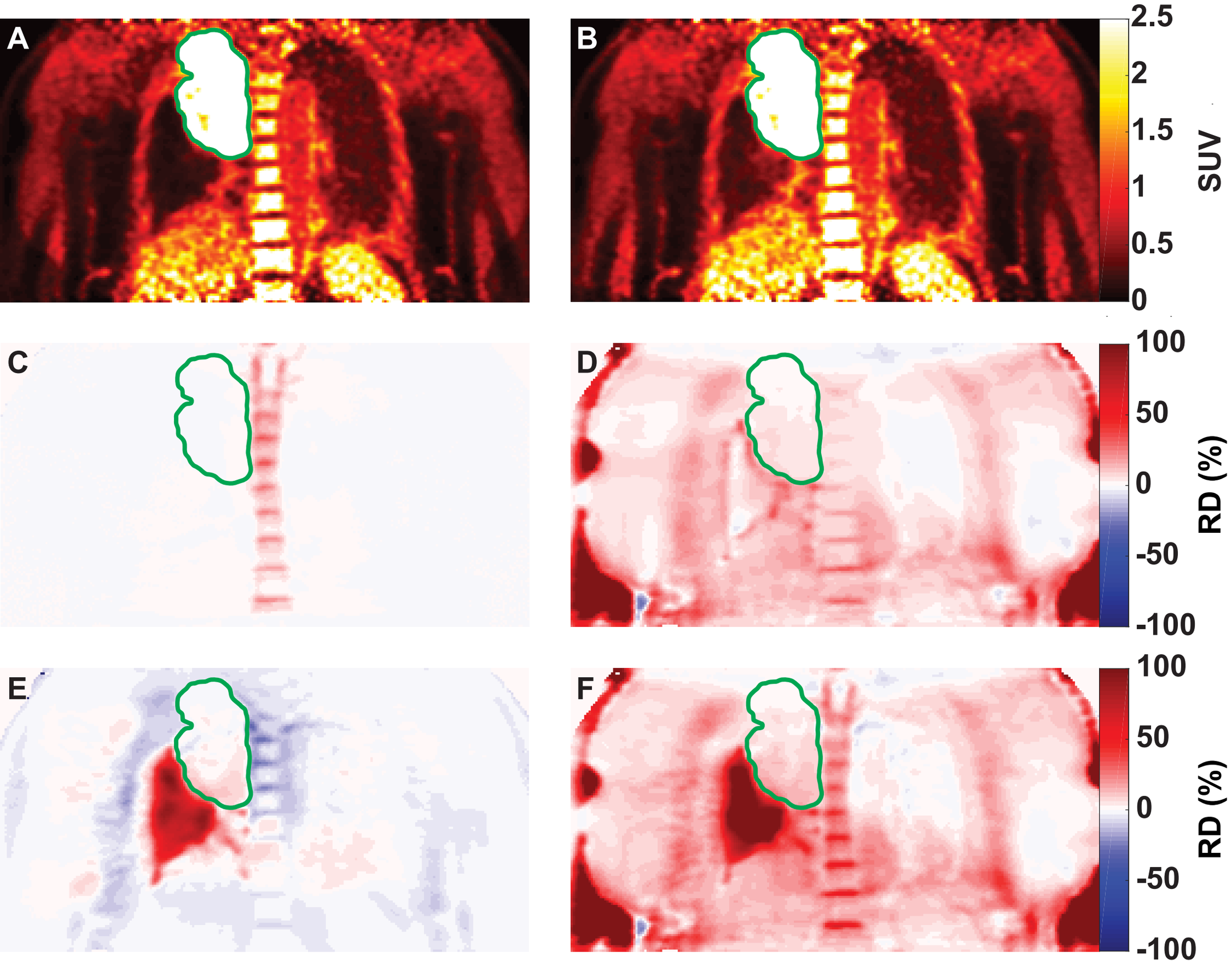
A
B
2.5
2
1.5
1
0.5
0
SUV
C
D
100
50
0
-50
-100
RD (%)
E
F
100
50
0
-50
-100
RD (%)

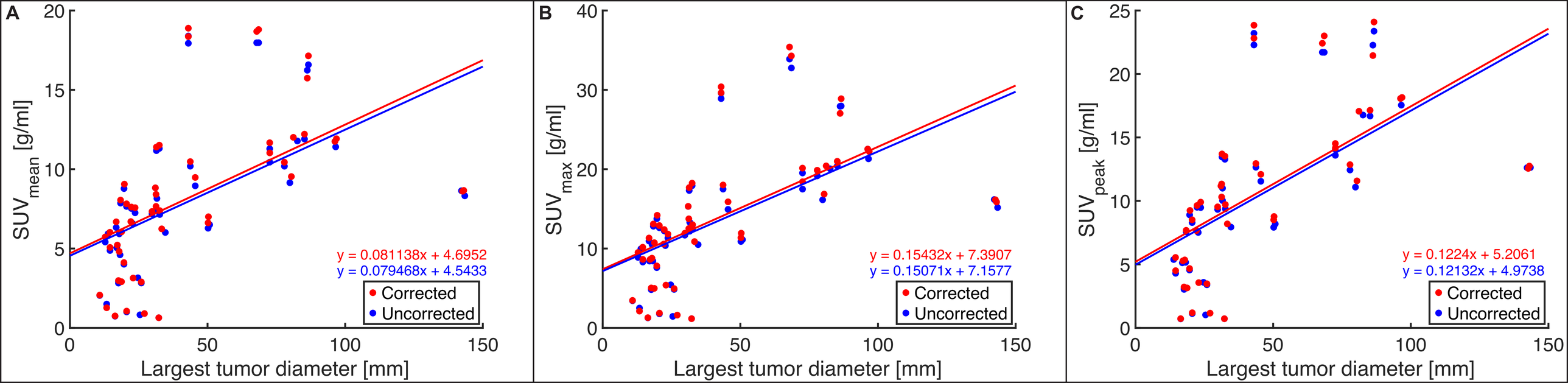
A
SUV mean [g/ml]
Largest tumor diameter [mm]
y = 0.081138x + 4.6952
y = 0.079468x + 4.5433
Corrected
Uncorrected
B
SUV max [g/ml]
Largest tumor diameter [mm]
y = 0.15432x + 7.3907
y = 0.15071x + 7.1577
Corrected
Uncorrected
C
SUV peak [g/ml]
Largest tumor diameter [mm]
y = 0.1224x + 5.2061
y = 0.12132x + 4.9738
Corrected
Uncorrected

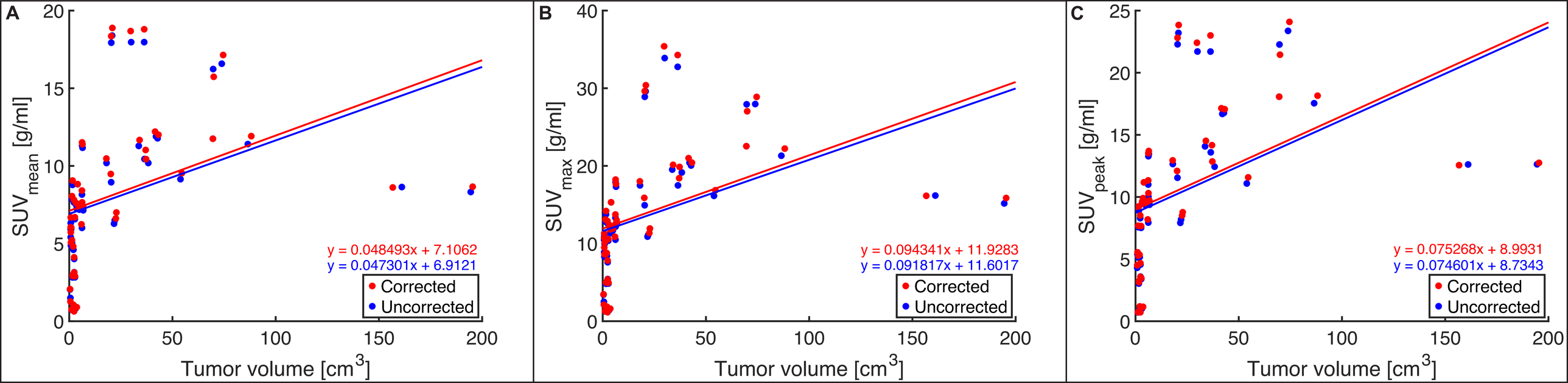
A
SUV mean [g/ml]
Tumor volume [cm3]
y = 0.048493x + 7.1062
y = 0.047301x + 6.9121
Corrected
Uncorrected
B
SUV max [g/ml]
Tumor volume [cm3]
y = 0.094341x + 11.9283
y = 0.091817x + 11.6017
Corrected
Uncorrected
C
SUV peak [g/ml]
Tumor volume [cm3]
y = 0.075268x + 8.9931
y = 0.074601x + 8.7343
Corrected
Uncorrected